

NIHAO XXV: Convergence in the cusp-core transformation of cold dark matter haloes at high star formation thresholds

Aaron A. Dutton^{1*}, Tobias Buck², Andrea V. Macciò^{1,3,4}, Keri L. Dixon^{1,4},
Marvin Blank^{1,4,5}, Aura Obreja⁶

¹*New York University Abu Dhabi, PO Box 129188, Saadiyat Island, Abu Dhabi, United Arab Emirates*

²*Leibniz-Institut für Astrophysik Potsdam (AIP), An der Sternwarte 16, D-14482 Potsdam, Germany*

³*Max Planck Institut für Astronomie, Königstuhl 17, 69117 Heidelberg, Germany*

⁴*Center for Astro, Particle and Planetary Physics (CAP³), New York University Abu Dhabi, United Arab Emirates*

⁵*Institut für Theoretische Physik und Astrophysik, Christian-Albrechts-Universität zu Kiel, Leibnizstr. 15, D-24118 Kiel, Germany*

⁶*University Observatory Munich, Scheinerstraße 1, D-81679 Munich, Germany*

Accepted 2020 September 28. Received 2020 September 28; in original form 2020 May 10

ABSTRACT

We use cosmological hydrodynamical galaxy formation simulations from the NIHAO project to investigate the response of cold dark matter (CDM) haloes to baryonic processes. Previous work has shown that the halo response is primarily a function of the ratio between galaxy stellar mass and total virial mass, and the density threshold above which gas is eligible to form stars, $n[\text{cm}^{-3}]$. At low n all simulations in the literature agree that dwarf galaxy haloes are cuspy, but at high $n \gtrsim 100$ there is no consensus. We trace halo contraction in dwarf galaxies with $n \gtrsim 100$ reported in some previous simulations to insufficient spatial resolution. Provided the adopted star formation threshold is appropriate for the resolution of the simulation, we show that the halo response is remarkably stable for $n \gtrsim 5$, up to the highest star formation threshold that we test, $n = 500$. This free parameter can be calibrated using the observed clustering of young stars. Simulations with low thresholds $n \leq 1$ predict clustering that is too weak, while simulations with high star formation thresholds $n \gtrsim 5$, are consistent with the observed clustering. Finally, we test the CDM predictions against the circular velocities of nearby dwarf galaxies. Low thresholds predict velocities that are too high, while simulations with $n \sim 10$ provide a good match to the observations. We thus conclude that the CDM model provides a good description of the structure of galaxies on kpc scales provided the effects of baryons are properly captured.

Key words: cosmology: theory – dark matter – galaxies: formation – galaxies: kinematics and dynamics – galaxies: structure – methods: numerical

1 INTRODUCTION

The structure of dark matter haloes on kiloparsec-scales provides a sensitive astrophysical test of the standard cold dark matter (CDM) paradigm, and more generally the nature of dark matter (e.g., Bullock & Boylan-Kolchin 2017). Through the use of dissipationless simulations, the structure of CDM haloes in the absence of baryons is well determined (e.g., Stadel et al. 2009; Dutton & Macciò 2014). The dissipation of gas to the center of haloes is thought to only make the dark matter halo contract (Blumenthal et al. 1986;

Gnedin et al. 2004). However, other baryonic processes can cause the dark matter halo to expand: dynamical friction from infalling baryonic clumps (El-Zant et al. 2001), resonances with galactic bars (Weinberg & Katz 2002), and multiple episodes of gas outflows (Read & Gilmore 2005; Pontzen & Governato 2012; Dutton et al. 2016b).

Using 10 cosmological galaxy formation simulations from the MAGICC project (Stinson et al. 2013), Di Cintio et al. (2014a) found that the structure of CDM haloes, and hence the trade off between gas inflows and outflows, depends on the ratio between the galaxy stellar mass and the halo mass $M_{\text{star}}/M_{\text{halo}}$ (which is proportional to the integrated star formation efficiency). At

* dutton@nyu.edu

low $M_{\text{star}}/M_{\text{halo}} \lesssim 0.0003$ the dark matter profile remains unchanged, due to minimal gas dissipation, and minimal gas outflows. As the efficiency increases the halo expansion gets stronger, while the contractive effect of inflows still remains small. The maximum expansion is reached at $M_{\text{star}}/M_{\text{halo}} \sim 0.003$. At higher $M_{\text{star}}/M_{\text{halo}}$ the expansion is reduced due to the increasing importance of gas inflows until above $M_{\text{star}}/M_{\text{halo}} \sim 0.03$ the halo contracts.

This result was confirmed by Tollet et al. (2016) using 60 simulations from the NIHAO project (Wang et al. 2015), and Chan et al. (2015); Bullock & Boylan-Kolchin (2017); Lazar, et al. (2020) using simulated galaxies from the FIRE (Hopkins et al. 2014) and FIRE-2 projects (Hopkins et al. 2018). See also Macciò, et al. (2020) for an extension to massive galaxies with AGN feedback. However, Bose et al. (2019) finds essentially no change in the dark matter halo for a wide range of $M_{\text{star}}/M_{\text{halo}}$ using the simulations from the AURIGA (Grand et al. 2017) and APOSTLE (Sawala et al. 2016) projects. The solution to this apparent contradiction is that the halo response is strongly dependent on the star formation density threshold adopted in the simulation (Governato et al. 2010; Dutton et al. 2019c; Benítez-Llambay et al. 2019). High thresholds $n \gtrsim 10$ can result in halo expansion (for suitable $M_{\text{star}}/M_{\text{halo}}$), while low thresholds $n \sim 0.1$ (e.g., APOSTLE, AURIGA) never result in significant halo expansion. While different simulation codes agree on the halo response at low $n \sim 0.1$, there is not yet consensus for high $n \gtrsim 100$ with Benítez-Llambay et al. (2019) finding dark halo contraction in dwarf galaxies, while FIRE, FIRE-2, Governato et al. (2010, 2012) and Read et al. (2016) finding halo expansion.

In order for hydrodynamical simulations of galaxy formation to make a robust prediction for the structure of CDM haloes we thus need to find ways to distinguish between simulations with different star formation thresholds. Dutton et al. (2019c) showed that simulations with different star formation thresholds resulted in differences in the variability in the star formation rates, with a factor ~ 2 more variability for $n = 10$ than $n = 0.1$. Buck et al. (2019b) showed that simulations with different star formation thresholds resulted in differences in the spatial distribution of young stars, specifically the two-point correlation. Comparing to observations of the two-point correlation of young star clusters from LEGUS (Grasha et al. 2017), Buck et al. (2019b) finds $n = 10$ consistent with observations, and $n = 1$ and $n = 0.1$ inconsistent, with clustering that is too weak.

In this paper we extend the studies of Dutton et al. (2019c) and Buck et al. (2019b) to an order of magnitude higher star formation thresholds with the goal of resolving the conflicting results at $n \gtrsim 100$. We also include a new set of simulations for $n = 0.1$ that we have recalibrated using the star formation efficiency, instead of the feedback efficiency.

This paper is organized as follows: The simulation suite is outlined in Section 2. Results on the convergence of the inner structure of CDM haloes are given in Section 3. In Section 4 we constrain the star formation threshold using the clustering of young stars. In Section 5 we test the CDM predictions with galaxy kinematics, finally a summary is given in Section 6.

2 SIMULATIONS

As in Dutton et al. (2019c), we use a set of 20 haloes of virial masses between $M_{200} \sim 10^{10}$ and $\sim 10^{12} M_{\odot}$ taken from the NIHAO project (Wang et al. 2015). NIHAO is a sample of $\simeq 100$ hydrodynamical cosmological simulations run using the SPH code GASOLINE2 (Wadsley et al. 2017). The uniqueness of NIHAO is in the combination of high spatial resolution over a wide range of halo masses (10^{10} to $10^{12} M_{\odot}$) for a statistical sample of haloes.

The masses and force softenings of the dark matter particles are chosen to resolve the mass profile at $\lesssim 1$ per cent of the virial radius, which results in $\sim 10^6$ dark matter particles inside the virial radius of all main haloes at $z = 0$. The corresponding masses and force softenings for the gas particles are a factor of $\Omega_b/\Omega_{\text{dm}} = 0.182$ and $\sqrt{\Omega_b/\Omega_{\text{dm}}} = 0.427$ lower. Each hydro simulation has a corresponding simulation of the same resolution, but with just dark matter particles (dark matter only, DMO) of the same resolution. These DMO simulations have been started using the identical initial conditions, replacing baryonic particles with dark matter particles.

As discussed in detail in previous papers, and as outlined below, NIHAO galaxies are consistent with a wide range of galaxy properties. They form the right amount of stars (as compared to halo abundance matching) both today and at earlier times (Wang et al. 2015). The masses and half-light sizes of the cold gas are consistent with observations (Stinson et al. 2015; Macciò et al. 2016). They follow several fundamental kinematic scaling relations: the gas, stellar, and baryonic Tully-Fisher relations (Dutton et al. 2017), and the radial acceleration relation (Dutton et al. 2019b). They match the clumpy morphology seen in observed galaxies at high redshifts (Buck et al. 2017). They reconcile the conflict between the steep halo velocity function of LCDM and the shallow HI linewidth velocity function observed in the nearby Universe (Macciò et al. 2016; Dutton et al. 2019a). They result in satellite mass functions resembling the one of the Milky Way (Buck, et al. 2019a), and emulate the Milky Ways central stellar bar (Buck, et al. 2018, 2019c). Given all of this success, they provide a good template with which to predict the structure of cold dark matter haloes.

We refer the reader to Wang et al. (2015) for a description of the NIHAO simulations and Dutton et al. (2019c) for more properties of the 20 resimulated galaxies. Here we briefly describe the parameters that we vary in this paper: the star formation threshold n , the efficiency of early stellar feedback, e_{ESF} , and the star formation efficiency, c_* .

In our simulations star formation is implemented as described in Stinson et al. (2006, 2013). Stars form from gas that is both cool ($T < 15000\text{K}$) and dense ($\rho > n[\text{cm}^{-3}]$). Gas that passes both thresholds is converted into stars according to

$$\frac{\Delta M_{\text{star}}}{\Delta t} = c_* \frac{M_{\text{gas}}}{t_{\text{dyn}}}. \quad (1)$$

Here ΔM_{star} is the mass of stars formed, $\Delta t = 0.84\text{Myr}$ is the time-step between star formation events (Age of Universe/ 2^{14}), and t_{dyn} is the gas particle's dynamical time. The fiducial efficiency of star formation is set to $c_* = 0.1$.

In our fiducial NIHAO simulations we adopt a star formation threshold of $n = 10[\text{cm}^{-3}]$. This is chosen as it is

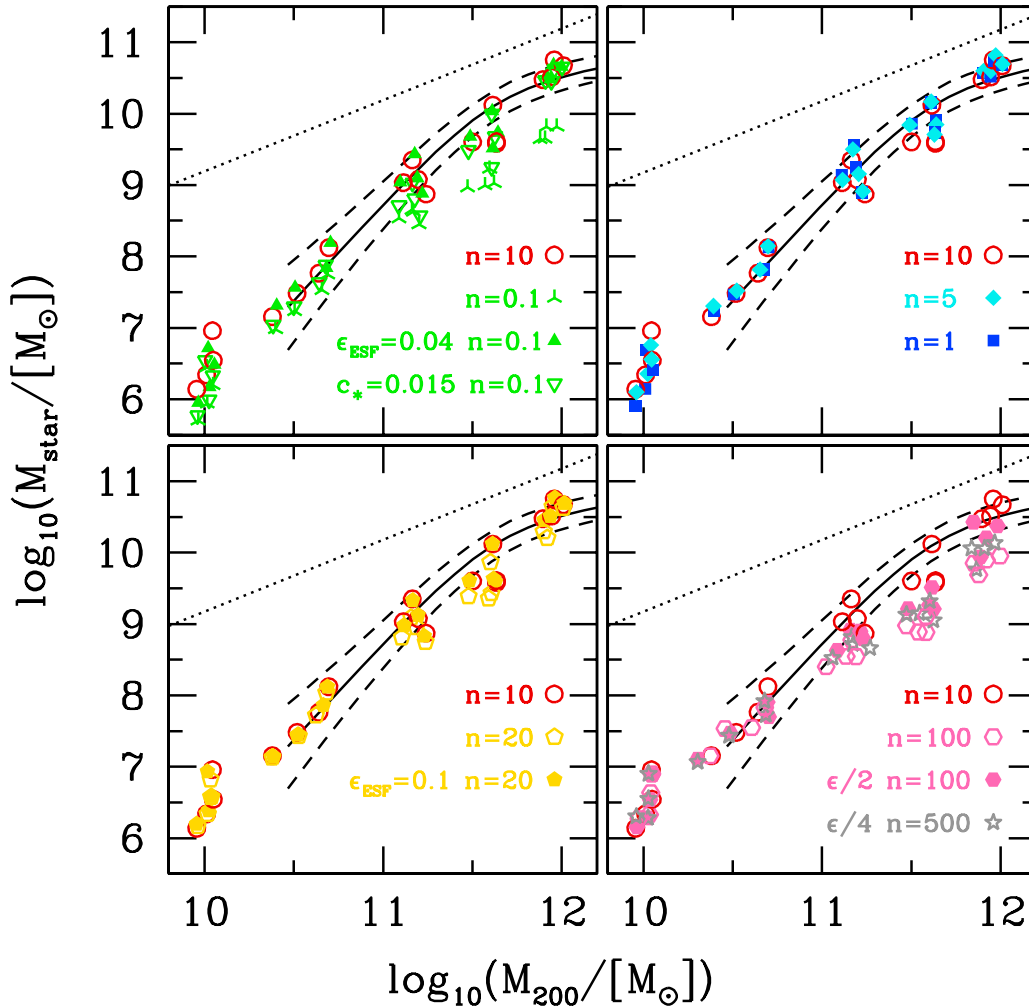


Figure 1. Relation between galaxy stellar mass, M_{star} , and total virial mass, M_{200} , at redshift $z = 0$. The solid and dashed lines show results (mean and 1σ scatter) from halo abundance matching (Moster et al. 2018), while the dotted line corresponds to the cosmic baryon fraction. Simulations with different star formation thresholds, n , are given in different colors: $n = 10$ (red, NIHAO default), $n = 0.1$ (green), $n = 1$ (blue), $n = 5$ (cyan), $n = 20$ (yellow), $n = 100$ (magenta), and $n = 500$ (grey). Some simulations have been recalibrated by varying the star formation efficiency, c_* , or the early stellar feedback efficiency, ϵ_{ESF} , with new parameters as indicated. At the highest n we include simulations with smaller force softenings: $\epsilon/2$, and $\epsilon/4$.

roughly the maximum density that we can resolve:

$$n_{\text{max}} \approx 50 m_{\text{gas}} / \epsilon_{\text{gas}}^3, \quad (2)$$

where m_{gas} is the gas particle mass and ϵ_{gas} is the gas gravitational force softening. Here 50 is the number of SPH particles in the smoothing kernel. For all our simulations (with different resolution levels) this formula results in the same $n_{\text{max}} \approx 10$.

In this paper we present new results for simulations with $n = 5$ and $n = 20$, as well as much higher values $n = 100$ and $n = 500$. As we will show below, in order to form galaxies with realistic baryonic mass distributions with $n \gg 10$ we need smaller force softenings. Smaller softening allows the gas to clump on smaller scales and thus reach higher densities (Eq. 2).

The other parameter of relevance to this study is the feedback efficiency. The NIHAO simulations employ ther-

mal feedback in two epochs as described in Stinson et al. (2013). The first epoch models the energy input from stellar winds and photoionization from bright young stars before supernovae explode. We thus term this early stellar feedback (ESF). The ESF consists of a fraction ϵ_{ESF} of the total stellar flux being ejected from stars into surrounding gas (2×10^{50} erg of thermal energy per M_{\odot} of the entire stellar population). Radiative cooling is left on for the ESF.

The second epoch models the energy input from supernovae and starts 4 Myr after the star forms. Stars with mass $8 M_{\odot} < M_* < 40 M_{\odot}$ eject both energy ($\epsilon_{\text{SN}} \times 10^{51}$ erg/SN) and metals into the interstellar medium gas surrounding the region where they formed. Supernova feedback is implemented using the blastwave formalism described in Stinson et al. (2006). To correct for numerical radiative losses, this model applies a delayed cooling formalism for particles inside the blast region for ~ 30 Myr.

The default parameters of the feedback model are $\epsilon_{\text{ESF}} = 0.13$ and $\epsilon_{\text{SN}} = 1.0$. They were calibrated against the evolution of the stellar mass versus halo mass relation from halo abundance matching (Behroozi et al. 2013; Moster et al. 2013) for a $z = 0$ Milky Way mass halo $\sim 10^{12} M_{\odot}$. In this paper we leave $\epsilon_{\text{SN}} = 1.0$ and vary ϵ_{ESF} .

2.1 Haloes and galaxies

Haloes are identified using the MPI+OpenMP hybrid halo finder AHF¹ (Gill et al. 2004; Knollmann & Knebe 2009). The virial mass of each halo is defined as the mass of all particles within a sphere whose average density is 200 times the cosmic critical matter density, $\rho_{\text{crit}} = 3H_0^2/8\pi G$. For the hydro simulations the virial mass, size and circular velocity of the haloes are denoted: M_{200} , R_{200} , V_{200} . For the DMO simulations the corresponding properties are denoted with a superscript, DMO. We define the stellar mass, M_{star} , of a galaxy to be the mass of stars enclosed within spheres of radius $r_{\text{gal}} = 0.2R_{200}$, corresponding to ~ 10 to ~ 50 kpc. consider the main halo per zoom-in simulation.

2.2 Feedback recalibration

Fig. 1 shows the ratio between stellar and virial mass at redshift $z = 0$ for the 20 main haloes. The solid (and dashed) lines are the mean (and scatter) from halo abundance matching from Moster et al. (2018), which we have corrected to our halo mass definition. Each panel shows results for $n = 10$ (fiducial NIHAO, red open circles) together with one or two other values of n . For $n = 1, 5$ and 10 the relation is very similar (top right panel). However, for both higher and lower n the fiducial simulation parameters under produce stars, especially so for the higher mass galaxies ($M_{200} > 10^{11} M_{\odot}$).

For $n = 0.1$ the fiducial parameters ($\epsilon_{\text{ESF}} = 0.13$, $c_* = 0.1$) result in stellar masses being under produced by an order of magnitude in the $M_{200} \sim 10^{12} M_{\odot}$ haloes. We recalibrate the $n = 0.1$ simulations in two ways: by reducing the efficiency of early-stellar feedback to $\epsilon_{\text{ESF}} = 0.04$ (filled triangles), or by reducing the star formation efficiency from $c_* = 0.1$ to $c_* = 0.015$ (open inverted triangles). The latter effect may seem counter-intuitive, since without feedback a lower c_* is expected to result in a lower stellar mass. However when feedback is included the opposite trend occurs. Feedback has the effect of heating gas and removing it from star forming regions, and thus naturally delays and reduces the amount of stars formed. Since denser gas radiates energy away faster, feedback is less efficient when the surrounding gas is denser. A lower c_* initially results in less star formation but also less feedback energy injected into the ISM, which results in denser gas. The denser gas reduces the efficiency of subsequent feedback events, and thus results in more gas available to form stars, and ultimately higher stellar masses.

For $n = 20$ the reduction in stellar mass is relatively small. We recalibrate by reducing the efficiency of early stellar feedback from $\epsilon_{\text{ESF}} = 0.13$ (open yellow pentagons) to $\epsilon_{\text{ESF}} = 0.10$ (filled yellow pentagons). The $n = 100$ simulations have a similar under production of stars as the $n = 0.1$

simulations. We have experimented with varying the feedback efficiency with limited success. The problem for these simulations is more fundamental than the choice of model parameters: they simply lack the spatial resolution to enable sufficient amounts of gas to locally reach the star formation threshold. For $n = 100$ we run simulations where all particles have half the force softening $\epsilon/2$ (filled magenta hexagons). For $n = 500$ we use one quarter of the standard softening $\epsilon/4$ (grey stars). The main effect of reducing the force softening is that it allows the smoothed gas densities to be higher (since we set the SPH smoothing length to be proportional to the gravitational force softening). A factor of 2 lower force softening thus allows a factor of 8 denser gas, and a factor of 4 lower force softening allows a factor of 64 denser gas. These haloes form significantly more stars than the standard softening simulations, yet they still under produce stars (in haloes with $M_{200} > 10^{11} M_{\odot}$) relative to the $n = 10$ simulations and halo abundance matching. So these simulations would benefit with further re-calibration of the feedback efficiency and/or star formation efficiency. We do note though that for dwarf galaxy haloes $10^{10} \lesssim M_{200} \lesssim 10^{11} M_{\odot}$ the stellar masses are remarkably insensitive to the star formation threshold and choice of force softening.

3 CONVERGENCE IN HALO RESPONSE AT HIGH STAR FORMATION THRESHOLD

The main result of this paper is shown in Fig. 2. This shows the change in the dark matter mass profile at 1 per cent of the virial radius (identical to the change in enclosed dark matter density), while the lower panel shows the slope of the enclosed dark matter density profile between 1 and 2 per cent of the virial radius. Note that here we use the enclosed dark matter density rather than the local dark matter density as used in our previous works (e.g., Tollet et al. 2016), but the results are qualitatively the same (compare the grey lines with the red circles).

In the upper panels, the dashed line corresponds to the DMO simulation (by definition), while in the lower panels the open circles show the DMO simulations (which cluster close to the NFW slope of -1). Results are shown versus stellar-to-halo mass ratio as this parameter has been shown to be better correlated with the halo response (Di Cintio et al. 2014a; Dutton et al. 2016b; Bullock & Boylan-Kolchin 2017) than either the stellar mass or halo mass alone.

For the lowest star formation threshold simulations $n = 0.1$ (green triangles) the haloes are essentially unchanged for $M_{\text{star}}/M_{200} \lesssim 10^{-2}$, while they contract for higher M_{star}/M_{200} due to the increased dissipation of gas. We show three sets of simulations for $n = 0.1$: the fiducial early stellar feedback efficiency $\epsilon_{\text{ESF}} = 0.13$ (pronged green triangles), $\epsilon_{\text{ESF}} = 0.04$ (solid green triangles), and $c_* = 0.015$ (open green triangles). All three sets of simulations show the same trend of halo response with M_{star}/M_{200} . These results for $n = 0.1$ are very similar to those for the APOSTLE and AURIGA simulations presented by Bose et al. (2019). This agreement is encouraging given the numerous differences between the codes. It suggests that how supernova feedback is modeled as well as the hydrodynamical scheme are of secondary importance compared to the star forma-

¹ <http://popia.ft.uam.es/AMIGA>

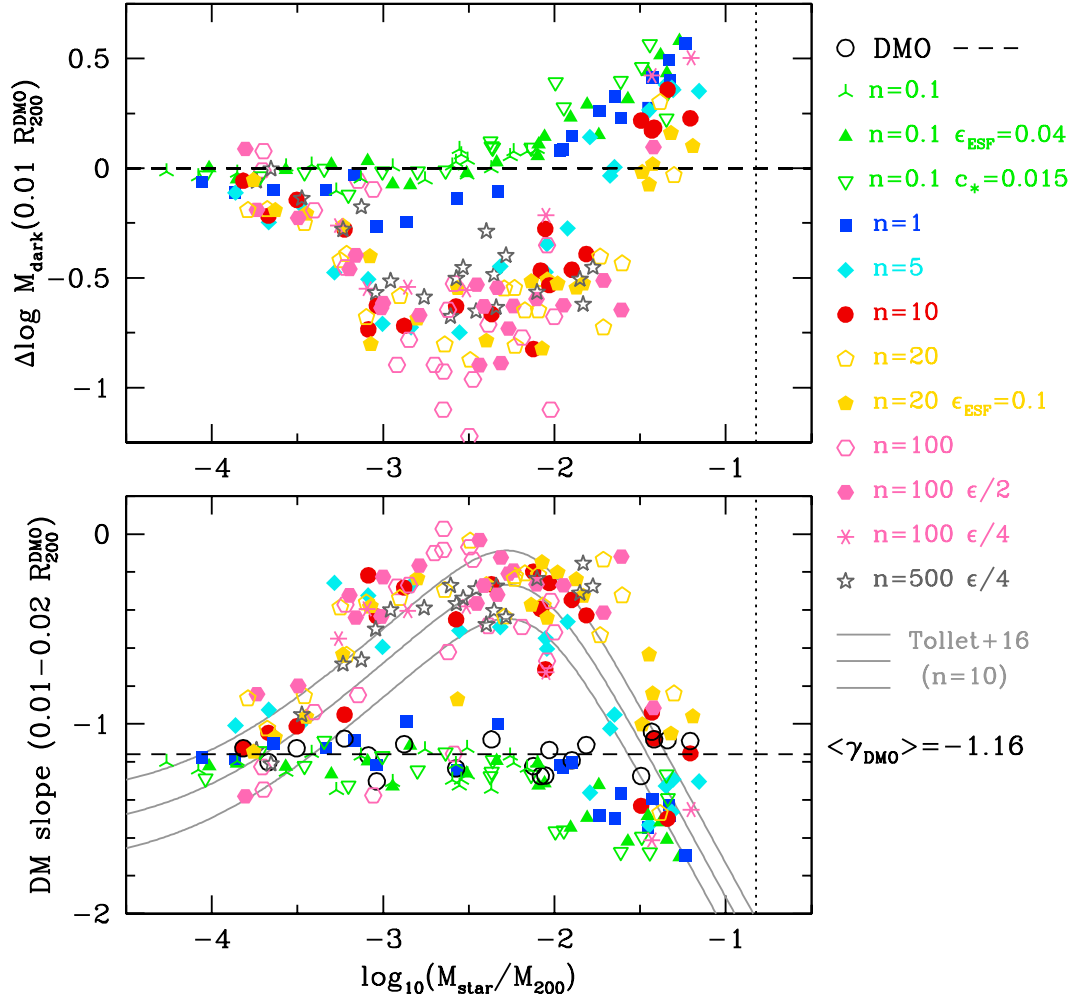


Figure 2. Change in enclosed mass ($\Delta \log M_{\text{dark}} \equiv \log M_{\text{dark}}^{\text{hydro}} - \log M_{\text{dark}}^{\text{DMO}}$) at 1 per cent of the virial radius (upper panels) and slope of the enclosed dark matter density profile between 1 and 2 per cent of the virial radius (lower panels) versus stellar to halo mass ratio. The dotted vertical line corresponds to the cosmic baryon fraction. The grey lines in the lower panel show the result from the full NIHAO sample from Tollet et al. (2016). The star formation threshold varies from $n = 0.1$ to $n = 500$ with colors and symbols as indicated. The default parameters are: efficiency of early stellar feedback $\epsilon_{\text{ESF}} = 0.13$, star formation efficiency $c_* = 0.1$. The halo response converges for $n \gtrsim 5$ provided the force softening is small enough.

tion threshold. Furthermore, we know of no cosmological galaxy formation simulation that contradicts this result. We thus conclude the lack of halo expansion for simulations run with low star formation thresholds $n \sim 0.1$ is a robust theoretical result. As discussed previously, and also below, if low-mass CDM haloes do not expand then the so-called too-big-to-fail problem for field galaxies represents a serious challenge for the CDM model (Garrison-Kimmel et al. 2014; Dutton et al. 2016a, 2019c).

As we increase the star formation threshold to $n = 1$ (blue squares) the trends are similar to that from $n = 0.1$, but with slightly shallower DM slopes and slight halo expansion. By $n = 5$ (cyan diamonds) strong halo expansion occurs when $10^{-3} \lesssim M_{\text{star}}/M_{200} \lesssim 10^{-2}$, while haloes still contract for $M_{\text{star}}/M_{200} \sim 10^{-1.5}$. For high thresholds $n = 10$ (red filled circles), $n = 20$ (yellow pentagons), $n = 100$ (magenta hexagons), and $n = 500$ (grey stars) the halo response

appears to have converged with strong expansion to dark matter cores for $10^{-3} \lesssim M_{\text{star}}/M_{200} \lesssim 10^{-2}$.

The concept of convergence in halo response is complicated because in our simulations halo expansion is primarily caused by feedback driven gas outflows. These occur during bursts of star formation. The timing of these bursts is not identical in different simulations run with identical initial conditions due to the stochastic nature of star formation in our simulations. Thus when we talk about convergence we focus on quantities averaged over several time steps and/or simulations with a given halo mass today.

The convergence in halo response at high star formation thresholds is shown for four individual haloes in Fig. 3. The vertical axis shows the ratio between enclosed dark matter masses in the hydro and DMO simulations at 1 per cent of the virial radius (i.e., the same parameter as in the upper panel of Fig. 2). For each simulation we show the results

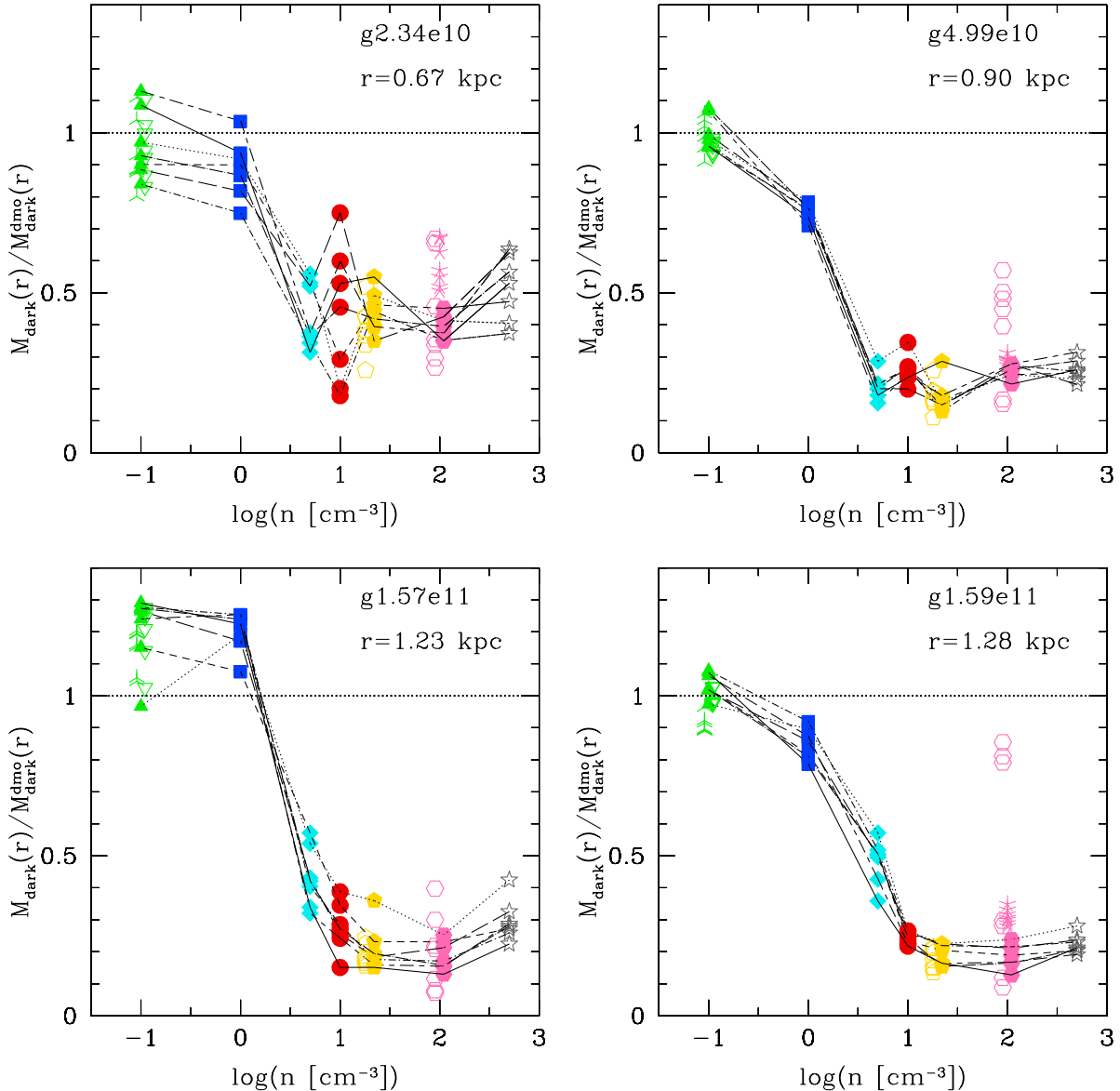


Figure 3. Ratio between dark matter mass in hydro and DMO simulations measured at 1 per cent of the virial radius versus the star formation threshold of the simulation. Point types and colors are as in Fig. 2. For thresholds with more than one set of simulations ($n = 0.1, n = 20, n = 100$) we have introduced small horizontal offsets for clarity. For each simulation we show 7 outputs equally spaced in time between redshifts $z = 0.5$ and $z = 0.0$. The lines connect simulations at a given redshift, where solid is $z = 0$. The average halo response converges for $n \gtrsim 10$.

of seven snapshots equally spaced in time between redshifts $z = 0.5$ and $z = 0$. This shows that for a given halo there is significant variability in the halo structure as a function of time. This variability is due to a combination of stochastic processes and systematic evolution. Nevertheless, if we look at the trends we see a strong difference in the average halo response between $n = 1$ (blue squares) and $n = 5$ (cyan diamonds). For $n \geq 10$ the halo response shows good convergence for a given halo. By convergence we mean the average dark matter mass is independent of n . The exception is that for $n = 100$ we see a larger variation in the halo response for the fiducial softening simulations (open hexagons) versus the half-softening simulations (filled hexagons). For $g1.59e11$ we

even see a few snapshots with mass ratios close to unity. We trace the origin of this feature in the $n = 100$ simulations to insufficient spatial resolution. When the star formation threshold is less than $n_{\text{max}} \simeq 10 [\text{cm}^{-3}]$ (for our fiducial resolution simulations) gas can locally fragment and thus turn into stars, the resulting feedback pushes gas out preventing a build up of gas in the galaxy center. When the threshold is higher than n_{max} , instead of forming stars, the gas loses angular momentum and collapses to the center of the galaxy until it is globally above the star formation threshold. A large starburst and gas outflow event follows, and then the process repeats.

An illustration of this is shown for halo $g1.59e11$ in

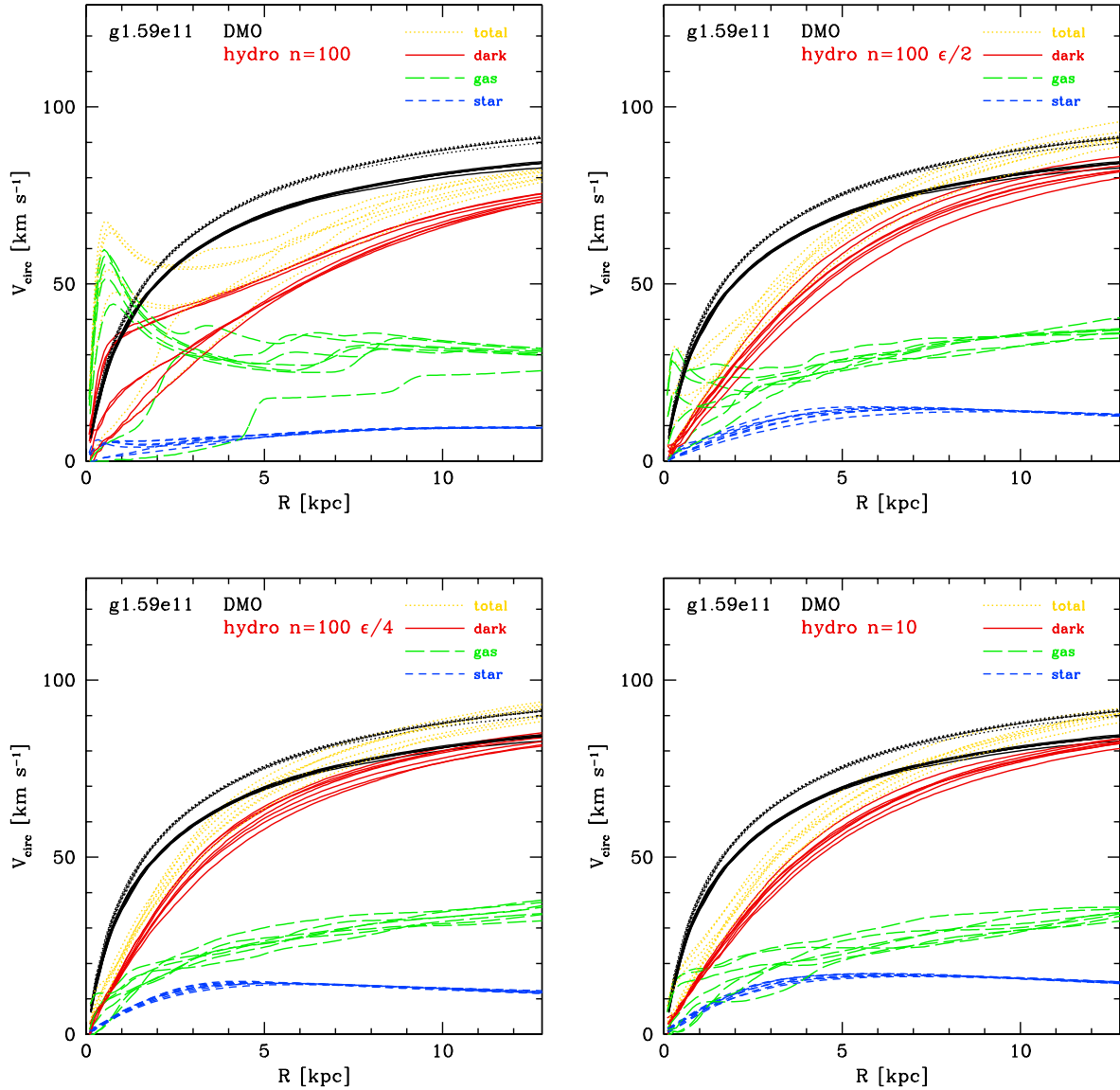


Figure 4. Effect of force softening on galaxy circular velocity profiles for g1.59e11. We show 7 outputs equally spaced in time between redshifts $z = 0.5$ and $z = 0.0$. In each panel the black lines show the DMO simulation: total (dotted) and scaled by $(\Omega_m - \Omega_b)/\Omega_m$ (solid). The colored lines show the hydro simulation. The DMO simulation has a very stable velocity profile. The $n = 10$ (lower right), $n = 100$ quarter softening (lower left), and $n = 100$ half-softening (upper right) simulations have similar stellar (blue lines), gas (green lines), dark matter (red lines) and total (yellow lines) profiles. In particular, the dark matter profiles show only small variation and noticeable expansion with respect to the DMO. By contrast the $n = 100$ (upper left) simulation has a high variability in the dark matter profiles at small radii, which can be traced to the high variability in the gas profile at small radii.

Fig. 4. Each panel shows the circular velocity profiles for seven snapshots equally spaced in time between redshift $z = 0.5$ and $z = 0$. For our standard simulations $n_{\max} = 10$ (lower right) the stellar (blue), gas (green), and dark matter (red) profiles are fairly stable, and the dark matter has expanded relative to the DMO (black lines) show the total (dotted) and “dark” (solid) components. For $n = 100$ (upper left) there is a wide variation in the gas profile. In some snapshots the gas is very concentrated, while in others the gas has been blown out of the galaxy center. As would be expected the dark matter variation follows the variation in

the gas (i.e., when the gas is more concentrated the dark matter is more concentrated). In some snapshots the dark matter profile even follows the DMO at small radii ($< \text{kpc}$). Since $n_{\max} \ll 100$ for our fiducial choice of m_{gas} and ϵ_{gas} we do not expect this simulation to be physically realistic.

This problem with $n = 100$ simulations can be simply fixed by reducing the force softening of the particles. When we reduce the force softening of the particles by a factor of 2 ($n_{\max} \simeq 80$, upper right) and a factor of 4 ($n_{\max} \simeq 640$, lower left) the resulting profiles (of the stars, gas, and dark matter) are very similar to that of the $n = 10$

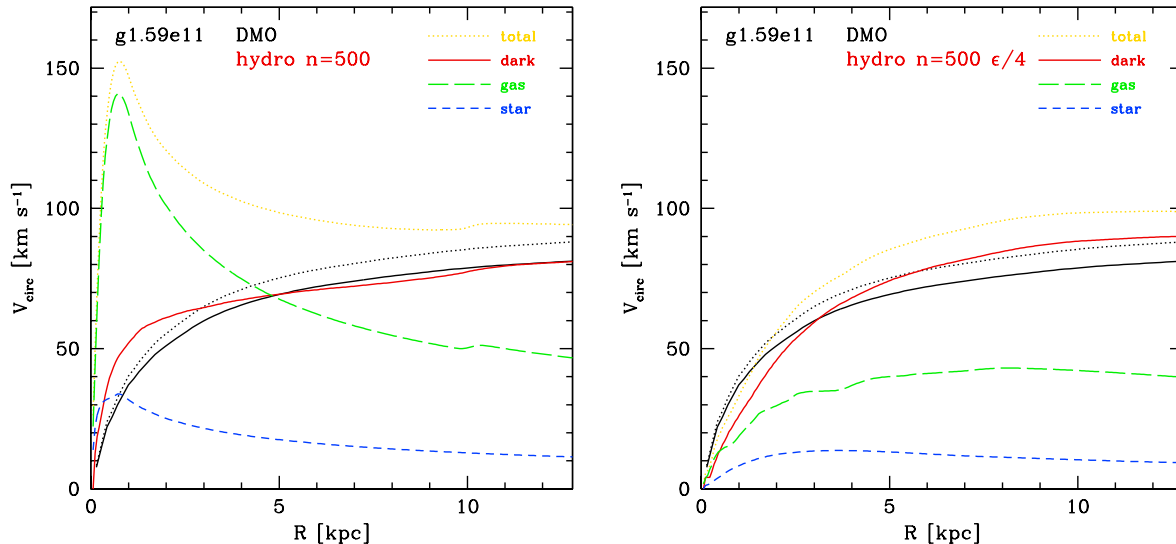


Figure 5. Effect of force softening on galaxy and halo mass profiles for halo g1.59e11 at $z = 1.47$. Both simulations have a star formation threshold of $n = 500$. With the fiducial force softening (left panel) the gas profile (green long-dashed) is very concentrated, and dominates the total mass within 4 kpc. This results in the dark matter profile (red solid) contracting with respect to the DMO simulation (black solid). With a force softening reduced by a factor of 4 (right panel), the gas profile is normal and the dark matter halo has started to expand within 3 kpc.

simulations. We note that these smaller force softenings are within the bounds set by Ludlow, Schaye & Bower (2019), see their fig. 1. Note also that there has been no recalibration of these simulations.

Fig. 5 shows the same halo but at an earlier time ($z = 1.47$) and now with $n = 500$. The standard softening run (upper left) now has an extremely overcooled gas bulge, which dominates the central potential and has resulted in dark halo contraction (the solid red line is above the solid black line below 5 kpc). The dense gas bulge also makes the simulation much slower to run, which is why we stopped it at high-redshift. The $n = 500$ quarter softening run (right) has similar star, gas, and dark matter profiles to the $n = 100$ quarter softening and $n = 10$ simulations. These simulations are all still dark matter dominated at small radii, and the inner dark matter halo has expanded compared to the DMO case.

Benítez-Llambay et al. (2019) showed that the inner dark matter content of low-mass haloes (and the size of their cores) is very sensitive to the assumed star formation threshold in the EAGLE model, hindering robust model predictions and the interpretation of observational data. The dwarf galaxy simulations of Benítez-Llambay et al. (2019) have $m_{\text{gas}} = 6.6 \times 10^4 M_{\odot}$ and $\epsilon_{\text{gas}} = 234$ pc, which results in $n_{\text{max}} = 10.5$ (i.e., almost identical to our fiducial simulations). Their halo response is stable for $n = 10$ to $n = 80$. For $n = 160$ they start to see the effects of overcooling. By $n = 320$ and $n = 640$ the gas dominates the central potential and the dark matter halo contracts. Their results are thus completely consistent with what we present here for our fiducial force softening runs.

Benítez-Llambay et al. (2019) suggest that it is the inefficiency of supernova feedback at higher gas densities in the EAGLE code (Crain et al. 2015) that is responsible for

the increased central gas densities when adopting a higher star formation threshold. They suggest that the numerical implementation of feedback will be important at high gas densities since this (over-cooling) effect does not occur in the FIRE-2 (Hopkins et al. 2018) galaxies which adopt a very high threshold of $n \sim 1000$.

Our results suggest a much simpler explanation, namely that the force softening used by Benítez-Llambay et al. (2019) is not appropriate for star formation thresholds significantly greater than $n \sim 10$. Indeed, the FIRE-2 (Fitts, et al. 2017) simulations are able to form galaxies with normal looking gas profiles with $n \sim 1000$ simply because they adopt very small force softenings (~ 20 times smaller than fiducial NIHAO for a given particle mass)².

To summarize, the response of dark matter haloes to galaxy formation is sensitive to the star formation threshold. However, the dependence on star formation threshold is quite simple, and is converged: at low thresholds $n \lesssim 1$ dwarf galaxy haloes essentially follow the DMO predictions, while for $n \gtrsim 10$ haloes expand for $0.001 \lesssim M_{\text{star}}/M_{200} \lesssim 0.01$.

4 CONSTRAINING THE STAR FORMATION THRESHOLD WITH OBSERVATIONS

Having established how the structure of dark matter haloes depends strongly on the star formation threshold we now turn to observations to calibrate this free parameter. Since our ultimate goal is to use these calibrated simulations to

² Fitts, et al. (2017) use $\epsilon_{\text{gas}} = 2$ pc for $m_{\text{gas}} = 500 M_{\odot}$. Compare this to $\epsilon_{\text{gas}} = 89.4$ pc for $m_{\text{gas}} = 3474 M_{\odot}$ for NIHAO, which scales to $\epsilon_{\text{gas}} = 46.9$ pc for $m_{\text{gas}} = 500 M_{\odot}$.

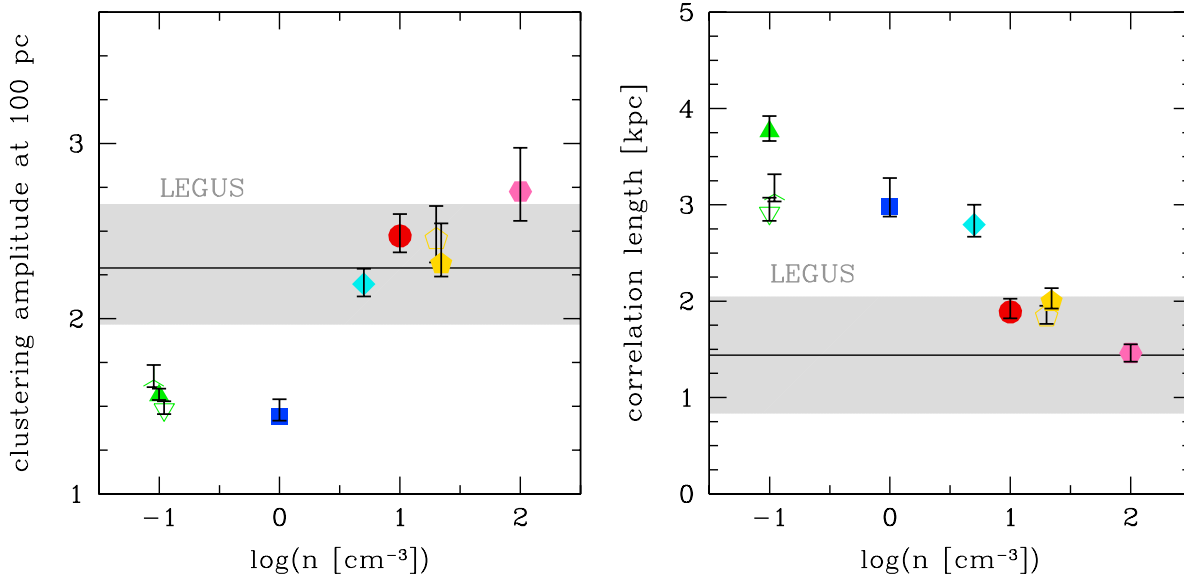


Figure 6. Clustering of young stars vs star formation threshold for galaxies with stellar masses $2 \times 10^8 \lesssim M_{\text{star}} \lesssim 3 \times 10^{10} M_{\odot}$. The left panel shows the clustering strength at 100 pc, $[1 + \xi(r = 100\text{pc})]$, while the right panel shows the correlation length, $r(\xi = 0)$. The shaded region shows observational results from LEGUS (Grasha et al. 2017). Colored points show the simulation median with error bars indicating the uncertainty on the median. Low star formation thresholds ($n \leq 1$) are disfavored by more than 2σ .

test the CDM model, we want to use observations that are not directly related to the structure of dark matter haloes.

Buck et al. (2019b) showed that the clustering of young stars in the NIHAO simulations depends strongly on the adopted star formation threshold. The clustering can be quantified using the two-point-correlation statistic of young star particles. Here we repeat the analysis of Buck et al. (2019b) using more values of the star formation threshold ($n = 5, n = 100$). To match the stellar mass range of the observed galaxies in Grasha et al. (2017) we take the 8 simulations with redshift $z = 0$ stellar masses $2 \times 10^8 \lesssim M_{\text{star}} \lesssim 3 \times 10^{10} M_{\odot}$. We use 24 snapshots evenly spaced in time from $z = 0.5$ to $z = 0.0$. For each snapshot we calculate the two-point-correlation statistic vs separation and fit the data with a function (see Buck et al. 2019b, for details). From the fit we calculate the clustering amplitude at a separation of 100 pc, and the radius where the clustering amplitude is equal to unity (i.e., that of a random distribution). For each set of simulations with a given n we find the median and scatter of the ~ 200 outputs.

Fig. 6 shows the clustering amplitude at 100 pc (left) and the correlation length (right) versus the star formation threshold of the simulation. The grey bands show the 1σ region of the observations using data from the LEGUS survey presented in Grasha et al. (2017). Note that in making this comparison we are assuming a correspondence between the clustering of observed young star clusters and the clustering of young simulated star particles. For the observations we use results for ages less than 40 Myr and all classes 1,2,3. In the simulations we only apply an age cut. The star particles in our simulations have similar masses as the observed star clusters ($\sim 10^3$ to $\sim 10^4 M_{\odot}$). Thus to a first order approximation our assumption that young star particles trace young stellar clusters seems reasonable. However, an in depth investigation into the correspondence between the clustering

of simulated star particles and observed star clusters, and ways to reduce any biases is certainly warranted.

For each simulation the symbol shows the median value, while the error-bar shows the error on the median ($1/\sqrt{N}$ times the standard deviation). As expected there is a clear trend for stronger clustering (higher clustering amplitude and smaller correlation length) with higher star formation thresholds. The simulations with $n = 5, 10, 20, 100$ overlap with the observed clustering, while the simulations with $n = 0.1$ and $n = 1$ are more than 2σ away from the observations, with clustering that is too weak. The multiple points for $n = 0.1$ and $n = 20$ show that the clustering strength is not sensitive to the feedback or star formation efficiency.

In summary, the clustering of young stars provides strong constraints to the sub-grid model for star formation in our simulations. Star formation thresholds of $n \leq 1$ are strongly disfavored, while $10 \lesssim n \lesssim 100$ provides a good match to the observed clustering. Even though the clustering does not single out a specific value for the star formation threshold, it still provides a very useful constraint because a majority of the galaxy formation simulations in the literature adopt a low star formation threshold ($n \sim 0.1$). Furthermore, as shown in Dutton et al. (2019c) and below, the inner structure of the dark matter halo also depends on the star formation threshold.

5 TESTING CDM WITH GALAXY KINEMATICS

Having established how the structure of CDM haloes depends on the star formation threshold, and calibrated this free parameter using the clustering of young stars, we now turn to observations of galaxy circular velocities to test the resulting predictions for CDM. Following the analysis in

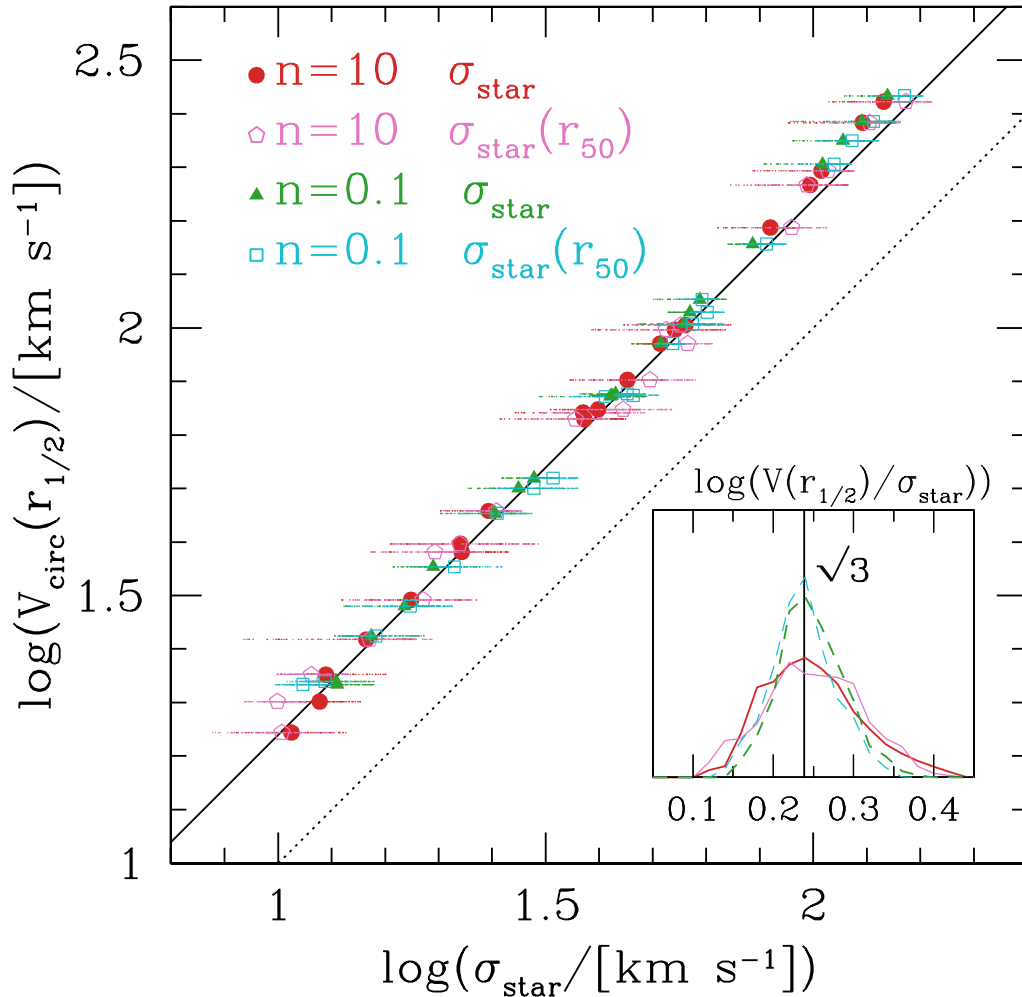


Figure 7. Circular velocity at the 3D half stellar mass radius vs the stellar velocity dispersion for simulations with $n = 10$ and $n = 0.1$. Small dots show single results from the 100 random projections. Large symbols show the median value for each galaxy. Filled symbols use the velocity dispersion of all the stars (within $0.2R_{200}$), open symbols use the velocity dispersion of the stars within the projected circular half stellar mass radius, R_{50} . The dotted line shows the 1:1 relation. The solid line shows the prediction from the virial theorem of $V_{\text{circ}}(r_{1/2}) = \sqrt{3}\sigma_{\text{star}}$, which is a good approximation in our simulations. The inset panel shows histograms of the ratio $V(r_{1/2})/\sigma_{\text{star}}$ which is approximately log-normally distributed with a standard deviation of about 0.04 (for $n = 0.1$) to 0.06 ($n = 10$) dex.

Dutton et al. (2019c) we split the tests into two mass ranges corresponding to dwarf galaxies ($10^6 \lesssim M_{\text{star}}/M_{\odot} \lesssim 10^8$) and intermediate-mass galaxies ($10^9 \lesssim M_{\text{star}}/M_{\odot} \lesssim 10^{10}$). This split is based on the availability of dynamical tracers. For the low-mass galaxies we use the integrated stellar velocity dispersions to trace the circular velocity within the half-light radius, while for the intermediate-mass galaxies we use resolved rotation curves.

First, we show that the projected stellar velocity dispersion, σ_{star} , is a good tracer of the circular velocity at the 3D stellar half-mass radius, $r_{1/2}$. Fig. 7 shows the relation between circular velocity and velocity dispersion for all 20 simulated galaxies at $z = 0$ using 100 random projections per galaxy. Red circles and magenta pentagons show results for $n = 10$, while green triangles and cyan squares show results for $n = 0.1$ (and re-calibrated with $\epsilon_{\text{ESF}} = 0.04$). Red and green points show the stellar velocity dispersion mea-

sured within the whole galaxy (defined to be 0.2 virial radii, R_{200}) while the magenta and cyan points show the stellar velocity dispersion within the projected stellar half-mass radius. Fig. 7 shows that the ratio between circular velocity and stellar velocity dispersion is, on average, insensitive to the star formation threshold of the simulation, and the aperture within which the velocity dispersion is measured.

On average we find $V_{\text{circ}}(r_{1/2}) = \sqrt{3}\sigma$, as predicted by the spherical Jeans equations (Wolf et al. 2010). There is a non-negligible scatter of $\simeq 0.06$ dex in this relation. The galaxy to galaxy variation is relatively small. Most of the scatter comes from variations resulting from different viewing angles. Thus samples of galaxies are needed to bring down the sampling errors.

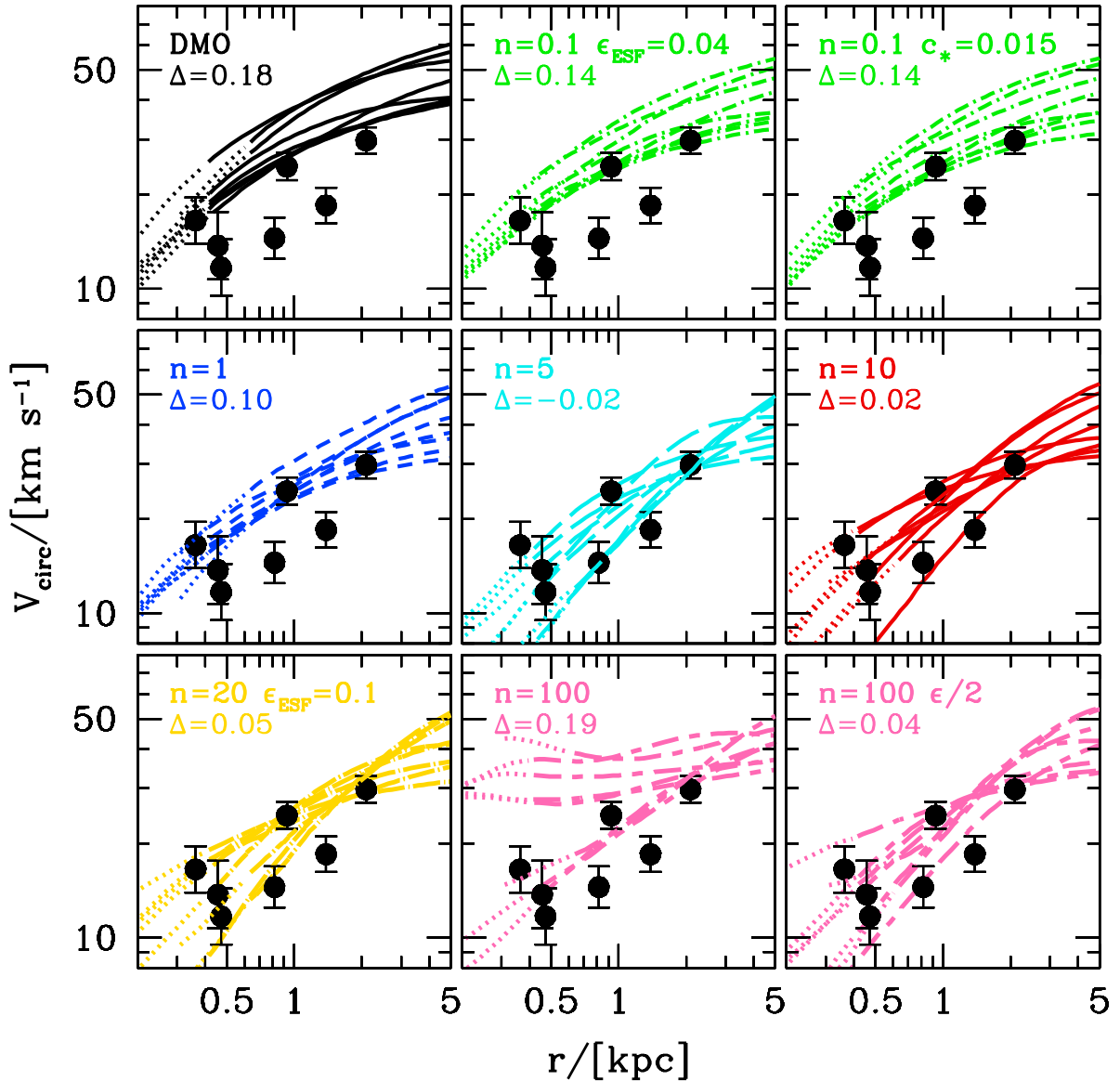


Figure 8. Circular velocity versus radius for dwarf galaxies with stellar masses $10^6 \lesssim M_{\text{star}} \lesssim 10^8 M_{\odot}$. Filled circles with error bars show observed field galaxies more than 500 kpc from the Milky Way (Kirby et al. 2014). Lines show our simulations, where the transition to dotted lines marks the scale that is accurately resolved (twice the dark matter softening). The parameter Δ is the mean offset (in dex) between the observations and the simulations. The DMO simulations (upper left) are offset from the observations by an average of 0.18 dex (i.e., a factor of 1.5). As the star formation threshold increases the offset decreases, such that with $n = 10$ (middle right) the offset is just 0.02 dex.

5.1 Dwarf galaxies

For the 8 lowest mass haloes in our sample in Fig. 8 we compare the simulated circular velocity profiles (lines) to the circular velocity at the 3D half-light radius of observed field dwarf galaxies in the Local Group (points with error bars) from Kirby et al. (2014). The simulated galaxies have stellar masses in the range $10^6 \lesssim M_{\text{star}} \lesssim 10^8 M_{\odot}$, while the observed dwarfs have with V-band luminosities from 10^6 to $2 \times 10^8 L_{\odot}$. In addition, for the observations we have excluded galaxies with distances less than 500 kpc (~ 2 virial radii) from the Milky Way to minimize contamination of back-splash galaxies (Buck, et al. 2019a). Note that four

panels in Fig. 8 have previously been published in fig. 4 of (Dutton et al. 2019c). The reproduced panels are: DMO (top left), $n = 0.1$ $\epsilon_{\text{ESF}} = 0.04$ (top center), $n = 1$ (middle left), and $n = 10$ (middle right). Here we reproduce these results and include five additional sets of simulations: $n = 0.1$ $c_* = 0.015$ (top right), $n = 5$ (middle center), $n = 20$ (lower left), $n = 100$ (lower center), and $n = 100$ with half force-softening (lower right).

As in Dutton et al. (2019c), we calculate the average offset between the observations (V_{obs}) and simulations (V_{sim}). For each observed data point, $V_{\text{obs},i}(r_{\text{obs},i})$, the mean offset

at radius $r_{\text{obs},i}$ with respect to the $N_{\text{sim}} = 8$ simulations is

$$\Delta_i = \frac{1}{N_{\text{sim}}} \sum_{j=1}^{N_{\text{sim}}} (\log_{10} V_{\text{obs},i}(r_{\text{obs},i}) - \log_{10} V_{\text{sim},j}(r_{\text{obs},i})) / N_{\text{sim}}. \quad (3)$$

We then take the mean of Δ_i over the 7 observed data points, which we denote Δ .

As previously shown in fig. 4 from [Dutton et al. \(2019c\)](#) we see that the DMO simulations (upper left panel) are systematically too high. The mean offset $\Delta = 0.18$, i.e. the average offset between simulation and observation is a factor of 1.5 in velocity, and a factor of 2.3 in enclosed mass. This recovers the well known too-big-to-fail problem of Local Group field galaxies ([Garrison-Kimmel et al. 2014](#)).

The lower threshold hydro simulations $n = 0.1$ ($\Delta = 0.14$) and $n = 1$ ($\Delta = 0.10$) can reproduce some, but not all of the observed data points, and predict circular velocities that are systematically too high. In particular for $n = 0.1$ the two sets of simulations show that the dark matter profiles are insensitive to the efficiencies of early stellar feedback and star formation.

We showed previously in [Dutton et al. \(2016a, 2019c\)](#) that the NIHAO simulations resolve the too-big-to-fail problem. The fiducial NIHAO $n = 10$ simulations match the observations well with $\Delta = 0.02$ (middle right panel). The new simulations ($n = 5$, recalibrated $n = 20$, and half-softening $n = 100$) also provide a good match to the observations which is interesting as these are the star formation thresholds that are consistent with the observed clustering of young stars shown above in Fig. 6. Notice that the $n = 100$ standard softening simulations result in a high $\Delta = 0.19$. This is due to the build up of gas in the galaxy centers (because the gas cannot easily reach the star formation threshold), rather than a strong contraction of the dark matter halo, or a significant stellar component. See the upper left panel in Fig. 4 for an example.

5.2 Intermediate-mass galaxies

We now consider the simulated galaxies with stellar masses in the range $10^9 \lesssim M_{\text{star}} \lesssim 10^{10} M_{\odot}$. As with the dwarf galaxies there are 8 haloes in this mass range. In Fig. 9 we compare the simulated circular velocity profiles (lines) to the dark matter circular velocity at the half-light radius (grey circles with error bars) from the SPARC survey of nearby star forming galaxies ([Lelli et al. 2016](#)). This figure extends the results previously shown in fig. 5 from [Dutton et al. \(2019c\)](#). Specifically the following panels are reproduced from [Dutton et al. \(2019c\)](#): DMO (top left), $n = 0.1$ $\epsilon_{\text{ESF}} = 0.04$ (top center), $n = 1$ (middle left), and $n = 10$ (middle right).

For observations the dark matter circular velocity is obtained by subtracting the stellar and gas circular velocity profile from the total rotation velocity, assuming a stellar mass-to-light ratio at $3.6 \mu\text{m}$ of 0.5. The solid black line shows the average velocity profile of the observations plotted between the average smallest and largest point on the rotation curve. Because these galaxies tend to be dark matter dominated, there is only a small uncertainty in the dark matter profile caused by the ~ 0.1 dex uncertainty in stellar mass-to-light ratio (dotted lines). Larger uncertainties

are how accurately the rotation curve corrected for inclination traces the circular velocity, and sampling effects since SPARC is not a volume limited survey.

The colored lines show the simulated dark matter circular velocity profiles computed in spheres: $V_{\text{circ}} = \sqrt{GM(<r)/r}$. For the DMO simulations the total profile has been rescaled by the cosmic baryon fraction ($\sqrt{1 - f_{\text{bar}}} \simeq 0.92$). For the hydro simulations symbols are located at the projected half-mass radius of the stars. This shows that the galaxy sizes for these simulations are in reasonable agreement with the observations and that there is only a small dependence of the sizes on the star formation threshold.

The parameter Δ (see Eq. 3) is computed at a radius of 2 kpc. This is chosen as it is the smallest spatial scale that is reliably resolved in both the simulations and observations for all galaxies. As with the dwarf galaxies in Fig. 8 we see that the DMO, $n = 0.1$ and $n = 1$ simulations are systematically too high, and as n increases the dark matter velocities are systematically reduced. The simulations that best match the observed clustering of young stars ($n \sim 10$), also provide the best match to the observations of dark matter circular velocities. Note that for $n = 100$ the under predicting of the observations is at least partly due to these simulations under producing stars (see Fig. 1). The $n = 100$ $\epsilon/2$ simulations do match the stellar masses for the dwarf galaxies, and also the velocities. So the apparent failure of the $n = 100$ $\epsilon/2$ simulations to match the velocities in Fig. 9 should not be considered a fatal failure of $n = 100$ simulations. A recalibration would thus be desirable before stronger conclusions for $n = 100$ are drawn.

A summary of the clustering and kinematic results is shown in Fig. 10. All the simulations shown here (except the $n = 100$ at intermediate masses) match the stellar mass vs halo mass relation (Fig. 1). The clustering measurements are used to provide further calibration. The upper panel shows the mean offset between the simulated and observed clustering (from Fig. 6) in units of the observed uncertainty. The error-bar connects the two measurements of clustering: amplitude at 100pc and correlation length. Except for $n = 5$ the two measurements give very similar results. The $n = 0.1$ and $n = 1$ simulations do not reproduce the observed clustering of young stars, and thus should not be used to test CDM. Simulations with $n = 10$ to $n = 100$ reproduce the clustering equally well. The $n = 5$ is consistent with only one measurement of clustering, making this threshold borderline successful.

The lower panel shows the mean offset in $\log V$ between simulations and observations (Δ parameter from Figs 8 & 9). This is used to test the CDM model. Again the vertical error-bars connect the two measurements for dwarf and intermediate-mass galaxies. The horizontal lines show the velocity offsets for the DMO simulations, which are quite close to the values for hydro simulations with $n = 1$ and $n = 0.1$. Thus DMO and hydro simulations with $n = 0.1$ and $n = 1$ fail to match observations. This is not a problem for CDM because these simulations have already been disfavored by the clustering measurements.

The red circle shows the fiducial NIHAO $n = 10$ which provides the best match to the clustering of young stars and circular velocities of nearby galaxies. We thus have shown that simulations that are calibrated to reproduce

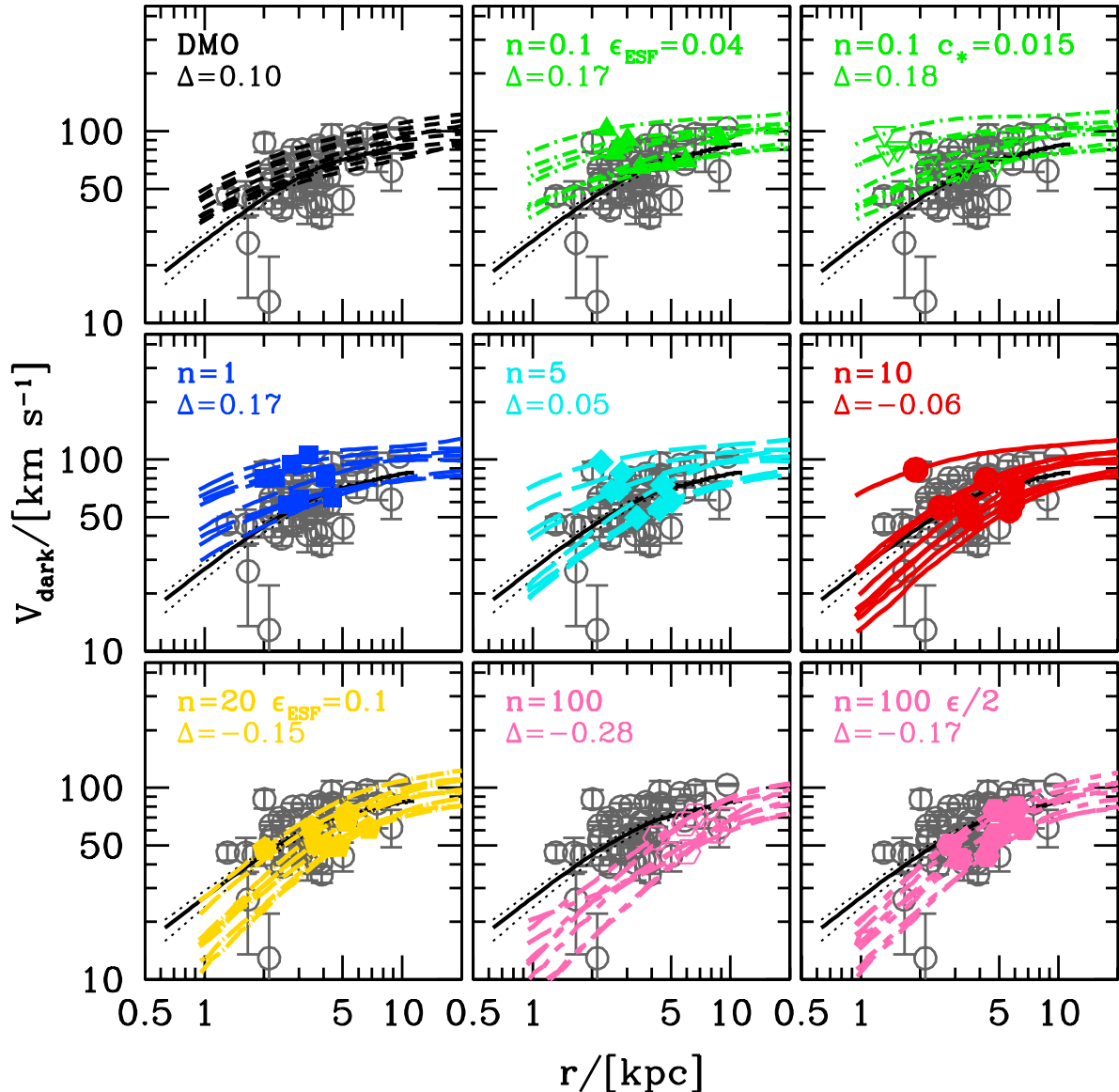


Figure 9. Dark matter circular velocity versus radius for galaxies with $10^{8.8} \lesssim M_{\text{star}} \lesssim 10^{10.2} M_{\odot}$. The same observations are shown in all panels. Grey circles with error-bars show the dark matter circular velocity at the half-light radius for observed galaxies from SPARC. The solid black line shows the mean dark matter circular velocity curve of the observations, while the dotted lines show the 1σ scatter. Each panel shows a different set of simulations with star formation threshold n as indicated. The points are located at the projected stellar half-mass radii. The value Δ is the mean offset [dex] between the simulations and the observed average velocity at 2 kpc.

both the stellar mass vs halo mass relation, and clustering of young stars, have dark matter on small scales consistent with CDM.

6 SUMMARY

In this paper we investigated the impact of the star formation threshold, n , on the response of the dark matter halo to galaxy formation. Extending the study of Dutton et al. (2019c) that looked at $n = 0.1, 1, 10$ here we consider thresholds as high as $n = 500$. As with Dutton et al. (2019c) we use 20 sets of cosmological hydrodynamical simulations from the NIHAO project (Wang et al. 2015) that simulate dark

matter haloes in the range $10^{10} \lesssim M_{200} \lesssim 10^{12} M_{\odot}$ at redshift $z = 0$. We summarize our results as follows:

- We confirm the results of previous studies that the response of the dark matter halo to galaxy formation is primarily a function of two parameters: 1) the ratio between stellar mass and halo mass (Di Cintio et al. 2014a; Chan et al. 2015; Tollet et al. 2016), and 2) the adopted star formation threshold, n , of the simulation (Dutton et al. 2019c; Benítez-Llambay et al. 2019).
- For high star formation thresholds ($n = 5$ to $n = 500$) the halo response has converged (Fig. 2), provided the simulation has sufficient spatial resolution to resolve the frag-

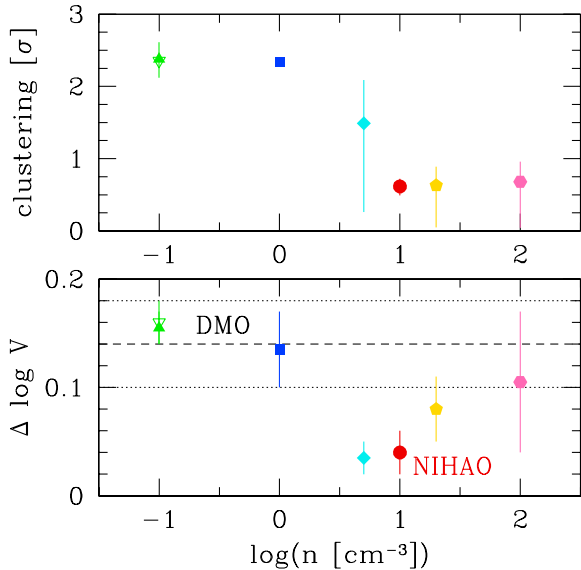


Figure 10. Summary of our results on the clustering of young stars (upper panel) and the circular velocities of nearby galaxies (lower panel) as a function of the star formation threshold of the simulations. The vertical error-bars show the range for two different measurements. In the lower panel the horizontal lines show the results for DMO simulations.

mentation of gas to densities above the gas density threshold in question.

- We trace previous claims by Benítez-Llambay et al. (2019) for halo contraction at $n \gtrsim 200$ to insufficient spatial resolution. With our default force softening the maximum gas density we can resolve is $n_{\max} \sim 10$. Applying our formula to the Benítez-Llambay et al. (2019) simulations also yields $n_{\max} = 10.5$. For our $n = 100$ and $n = 500$ simulations the gas is unable to locally fragment, instead it loses angular momentum and collapses to the center of the galaxy. The gas dominates the central potential causing the dark matter halo to contract (Fig.5). However, if we reduce the force softening of the gas by a factor of 2 to 4, we recover the halo expansion achieved from our fiducial $n = 10$ simulations using $n = 100$ (Fig. 4).

- Following Buck et al. (2019b) we use the spatial clustering of young stars to calibrate the star formation threshold parameter. The clustering strength increases roughly monotonically with star formation threshold (Fig. 6). Low threshold simulations ($n = 0.1$ to $n = 1$) are inconsistent with observations at more than 2σ , while simulations with $n = 10$ to $n = 100$ are consistent with observations (Fig. 10).

- Finally, to test the CDM model we use the circular velocity vs radius plot for galaxies with stellar masses $10^6 \lesssim M_{\text{star}} \lesssim 10^{10}$ (Figs. 8 & 9). DMO simulations and low star formation threshold simulations ($n = 0.1, n = 1$) fail by predicting a factor of $\simeq 2$ more mass than is observed. Simulations with $n \sim 10$ provide a good match to the observations.

- Investigating systematic effects in this test (for low-mass galaxies) we show that stellar velocity dispersions are an unbiased tracer of the circular velocity at the 3D stellar half-mass radius (Fig.7).

We thus conclude that the CDM model provides a good description of the structure of galaxies on kpc scales (once the effects of baryons are properly taken into account).

With our choice of sub-grid models, only simulations with a high star formation threshold can make accurate predictions for the structure of CDM haloes. As well as the fiducial NIHAO Wang et al. (2015) simulations several other groups also adopt a high star formation threshold: e.g., Governato et al. (2010, 2012), FIRE Hopkins et al. (2014, 2018), and Read et al. (2016). If this result extends to other choices of sub-grid models, it means that a large fraction of the zoom-in simulations in the literature: e.g., APOSTLE (Sawala et al. 2016), AURIGA (Grand et al. 2017); and all of the large volume simulations: e.g., EAGLE (Schaye et al. 2015), ILLUSTRIS (Vogelsberger, et al. 2014; Pillepich, et al. 2019), ROMULUS (Tremmel, et al. 2017) need to revise and re-calibrate their models for star formation and feedback if they are to make accurate predictions for the structure of cold dark matter haloes on kpc scales. An additional consideration is that simulations with higher star formation thresholds take significantly longer to run (due to the higher gas densities, and subsequent smaller required time steps). Many of the large volume simulations would not be computationally feasible at present if run with a high star formation threshold model. Thus there is a trade-off between the accuracy of the simulation and the number of haloes that can be simulated.

Looking to the future, both the calibration of the star formation threshold and the testing of CDM that we present are based on small samples of simulated and observed galaxies. Thus significant improvements in the accuracy are possible with larger samples. Improved accuracy will enable the framework we have presented to be applied to other models for dark matter, such as warm dark matter and self-interacting dark matter.

ACKNOWLEDGMENTS

We thank the anonymous referee for providing a constructive report that improved the clarity of the paper. This research was carried out on the High Performance Computing resources at New York University Abu Dhabi; on the THEO cluster of the Max-Planck-Institut für Astronomie and on the HYDRA clusters at the Rechenzentrum in Garching. The authors gratefully acknowledge the Gauss Centre for Supercomputing e.V. (www.gauss-centre.eu) for funding this project by providing computing time on the GCS Supercomputer SuperMUC at Leibniz Supercomputing Centre (www.lrz.de). TB acknowledges support from the European Research Council under ERC-CoG grant CRAGSMAN-646955. AO is funded by the Deutsche Forschungsgemeinschaft (DFG, German Research Foundation) – MO 2979/1-1.

DATA AVAILABILITY STATEMENT

The data underlying this article will be shared on reasonable request to the corresponding author.

REFERENCES

- Behroozi, P. S., Wechsler, R. H., & Conroy, C. 2013, *ApJ*, 770, 57
- Benítez-Llambay, A., Frenk, C. S., Ludlow, A. D., et al. 2019, *MNRAS*, 488, 2387
- Blumenthal, G. R., Faber, S. M., Flores, R., & Primack, J. R., 1986, *ApJ*, 301, 27
- Bose, S., Frenk, C. S., Jenkins, A., et al. 2019, *MNRAS*, 486, 4790
- Buck, T., Macciò, A. V., Obreja, A., et al. 2017, *MNRAS*, 468, 3628
- Buck T., Ness M. K., Macciò A. V., Obreja A., Dutton A. A., 2018, *ApJ*, 861, 88
- Buck T., Macciò A. V., Dutton A. A., Obreja A., Frings J., 2019a, *MNRAS*, 483, 1314
- Buck, T., Dutton, A. A., & Macciò, A. V. 2019b, *MNRAS*, 486, 1481
- Buck T., Ness M., Obreja A., Macciò A. V., Dutton A. A., 2019c, *ApJ*, 874, 67
- Bullock, J. S., & Boylan-Kolchin, M. 2017, *ARA&A*, 55, 343
- Chan, T. K., Kereš, D., Oñorbe, J., et al. 2015, *MNRAS*, 454, 2981
- Crain, R. A., Schaye, J., Bower, R. G., et al. 2015, *MNRAS*, 450, 1937
- Di Cintio, A., Brook, C. B., Macciò, A. V., et al. 2014, *MNRAS*, 437, 415
- Dutton, A. A., & Macciò, A. V. 2014, *MNRAS*, 441, 3359
- Dutton, A. A., Macciò, A. V., Frings, J., et al. 2016a, *MNRAS*, 457, L74
- Dutton, A. A., Macciò, A. V., Dekel, A., et al. 2016b, *MNRAS*, 461, 2658
- Dutton, A. A., Obreja, A., Wang, L., et al. 2017, *MNRAS*, 467, 4937
- Dutton, A. A., Obreja, A., & Macciò, A. V. 2019a, *MNRAS*, 482, 5606
- Dutton, A. A., Macciò, A. V., Obreja, A., et al. 2019b, *MNRAS*, 485, 1886
- Dutton, A. A., Macciò, A. V., Buck, T., et al. 2019c, *MNRAS*, 486, 655
- El-Zant, A., Shlosman, I., & Hoffman, Y. 2001, *ApJ*, 560, 636
- Fitts A., et al., 2017, *MNRAS*, 471, 3547
- Garrison-Kimmel, S., Boylan-Kolchin, M., Bullock, J. S., & Kirby, E. N. 2014, *MNRAS*, 444, 222
- Gill, S. P. D., Knebe, A., & Gibson, B. K. 2004, *MNRAS*, 351, 399
- Gnedin, O. Y., Kravtsov, A. V., Klypin, A. A., & Nagai, D. 2004, *ApJ*, 616, 16
- Governato, F., Brook, C., Mayer, L., et al. 2010, *Nature*, 463, 203
- Governato, F., Zolotov, A., Pontzen, A., et al. 2012, *MNRAS*, 422, 1231
- Grand, R. J. J., Gómez, F. A., Marinacci, F., et al. 2017, *MNRAS*, 467, 179
- Grasha, K., Calzetti, D., Adamo, A., et al. 2017, *ApJ*, 840, 113
- Hopkins, P. F., Kereš, D., Oñorbe, J., et al. 2014, *MNRAS*, 445, 581
- Hopkins, P. F., Wetzel, A., Kereš, D., et al. 2018, *MNRAS*, 480, 800
- Kirby, E. N., Bullock, J. S., Boylan-Kolchin, M., Kaplinghat, M., & Cohen, J. G. 2014, *MNRAS*, 439, 1015
- Knollmann, S. R., & Knebe, A. 2009, *ApJS*, 182, 608
- Lazar A., Bullock J. S., Boylan-Kolchin M., Chan T. K., Hopkins P. F., Graus A. S., Wetzel A., et al., 2020, *MNRAS*, 497, 2393
- Lelli, F., McGaugh, S. S., & Schombert, J. M. 2016, *AJ*, 152, 157
- Ludlow A. D., Schaye J., Bower R., 2019, *MNRAS*, 488, 3663
- Macciò, A. V., Udrescu, S. M., Dutton, A. A., et al. 2016, *MNRAS*, 463, L69
- Macciò A. V., Crespi S., Blank M., Kang X., 2020, *MNRAS*, 495, L46
- Moster, B. P., Naab, T., & White, S. D. M. 2013, *MNRAS*, 428, 3121
- Moster, B. P., Naab, T., & White, S. D. M. 2018, *MNRAS*, 477, 1822
- Pillepich A., et al., 2019, *MNRAS*, 490, 3196
- Pontzen, A., & Governato, F. 2012, *MNRAS*, 421, 3464
- Read, J. I., & Gilmore, G. 2005, *MNRAS*, 356, 107
- Read, J. I., Agertz, O., & Collins, M. L. M. 2016, *MNRAS*, 459, 2573
- Sawala, T., Frenk, C. S., Fattahi, A., et al. 2016, *MNRAS*, 457, 1931
- Schaye, J., Crain, R. A., Bower, R. G., et al. 2015, *MNRAS*, 446, 521
- Stadel, J., Potter, D., Moore, B., et al. 2009, *MNRAS*, 398, L21
- Stinson, G., Seth, A., Katz, N., et al. 2006, *MNRAS*, 373, 1074
- Stinson, G. S., Brook, C., Macciò, A. V., et al. 2013, *MNRAS*, 428, 129
- Stinson, G. S., Dutton, A. A., Wang, L., et al. 2015, *MNRAS*, 454, 1105
- Tollet, E., Macciò, A. V., Dutton, A. A., et al. 2016, *MNRAS*, 456, 3542
- Tremmel M., et al., 2017, *MNRAS*, 470, 1121
- Vogelsberger M., et al., 2014, *MNRAS*, 444, 1518
- Wang, L., Dutton, A. A., Stinson, G. S., et al. 2015, *MNRAS*, 454, 83
- Wadsley, J. W., Keller, B. W., & Quinn, T. R. 2017, *MNRAS*, 471, 2357
- Weinberg, M. D., & Katz, N. 2002, *ApJ*, 580, 627
- Wolf J., et al., 2010, *MNRAS*, 406, 1220